New constraints on a light *CP*-odd Higgs boson and related NMSSM ideal Higgs scenarios

Radovan Dermisek

Department of Physics, Indiana University, Bloomington, Indiana 47405, USA

John F. Gunion

Department of Physics, University of California, Davis, California 95616, USA,
and Theory Group, CERN, CH-1211, Geneva 23, Switzerland
(Received 11 February 2010; published 8 April 2010)

Recent *BABAR* limits on BR($\Upsilon(3S) \to \gamma a \to \gamma \tau^+ \tau^-$) and BR($\Upsilon(3S) \to \gamma a \to \gamma \mu^+ \mu^-$) provide increased constraints on the $ab\bar{b}$ coupling of a *CP*-odd Higgs boson, a, with $m_a < M_{\Upsilon(3S)}$. We extract these limits from the *BABAR* data and compare to the limits previously obtained using other data sets, especially the CLEO-III BR($\Upsilon(1S) \to \gamma \to \tau^+ \tau^-$) limits. Comparisons are made to predictions in the context of "ideal"-Higgs NMSSM scenarios, in which the lightest *CP*-even Higgs boson, h_1, can have mass below 105 GeV (as preferred by precision electroweak data) and yet can escape old LEP limits by virtue of decays to a pair of the lightest *CP*-odd Higgs bosons, $h_1 \to a_1 a_1$, with $m_{a_1} < 2m_B$. Most such scenarios with $m_{a_1} < 2m_\tau$ are eliminated, but the bulk of the $m_{a_1} > 7.5$ GeV scenarios, which are theoretically the most favored, survive. We also outline the impact of the new ALEPH LEP results in the $e^+ e^- \to Z + 4\tau$ channel. For $\tan\beta \gtrsim 3$, only NMSSM ideal Higgs scenarios with $m_{h_1} \gtrsim 98$ GeV and m_{a_1} close to $2m_B$ satisfy the ALEPH limits. For $\tan\beta \lesssim 2$, the ALEPH limits are easily satisfied for the most theoretically preferred NMSSM scenarios, which are those with m_{a_1} close to $2m_B$ and $m_{h_1} \sim$ 90–100 GeV.

I. INTRODUCTION

Many motivations for the existence of a light *CP*-odd *a* Higgs boson have emerged in a variety of contexts in recent years. Of particular interest is the $m_a < 2m_B$ region, for which a light Higgs, h, with SM-like *WW*, *ZZ*, and fermionic couplings can have mass $m_h \sim 100$ GeV while still being consistent with published LEP data by virtue of $h \to aa \to 4\tau$ or 4-jet decays being dominant [1–4] (see also [5,6]). Such a light Higgs provides perfect agreement with the rather compelling precision electroweak constraints, and for BR($h \to aa$) $\gtrsim 0.75$ also provides an explanation for the $\sim 2.3\sigma$ excess observed at LEP in $e^+ e^- \to Zb\bar{b}$ in the region $M_{b\bar{b}} \sim 100$ GeV. This is sometimes referred to as the "ideal" Higgs scenario. More generally, superstring modeling suggests the possibility of many light *a*'s. In this note, we update the analysis of [7] (see also [8]), quantifying the increased constraints on a general *CP*-odd *a* arising from recent *BABAR* limits on the branching ratio for $\Upsilon(3S) \to \gamma a \to \gamma \tau^+ \tau^-$ decays [9] and $\Upsilon(3S) \to \gamma a \to \gamma \mu^+ \mu^-$ decays [10]. We also quantify the impact of these constraints, as well as the impact of the new ALEPH LEP results in the $e^+ e^- \to Z + 4\tau$ final state [11], on the next-to-minimal supersymmetric model (NMSSM) ideal Higgs scenarios.

The possibilities for discovery of an *a* and limits on the *a* are phrased in terms of the $a\mu^- \mu^+$, $a\tau^- \tau^+$, $ab\bar{b}$, and $at\bar{t}$ couplings defined via

$$\mathcal{L}_{af\bar{f}} \equiv iC_{af\bar{f}} \frac{ig_2 m_f}{2m_W} \bar{f} \gamma_5 f a. \qquad (1.1)$$

(Note: when discussing a generic *CP*-even (*CP*-odd) Higgs boson, we will use the notation h (a). When specializing to the NMSSM context, we will use $h_1, h_2, h_3(a_1, a_2)$ for the mass ordered Higgs states.) In this paper, we assume a Higgs model in which $C_{a\mu^- \mu^+} = C_{a\tau^- \tau^+} = C_{ab\bar{b}}$, as typified by a two-Higgs-doublet model (2HDM) of either type I or type II, or more generally if the lepton and down-type quark masses are generated by the same combination of Higgs fields. However, one should keep in mind that there are models in which $r = (C_{a\mu^- \mu^+} = C_{a\tau^- \tau^+})/C_{ab\bar{b}} \gg 1$—such models include those in which the muon and tau masses are generated by different Higgs fields than the *b* mass. In a 2HDM of type II and in the MSSM, $C_{a\mu^- \mu^+} = C_{a\tau^- \tau^+} = C_{ab\bar{b}} = \tan\beta$ (where $\tan\beta = h_u/h_d$ is the ratio of the vacuum expectation values for the doublets giving mass to up-type quarks vs down-type quarks) and $C_{at\bar{t}} = \cot\beta$. These results are modified in the NMSSM (see, e.g. [12,13]).[1] In the NMSSM, both $C_{a_1 t\bar{t}}$ and $C_{a_1 b\bar{b}} = C_{a_1 \mu^- \mu^+} = C_{a_1 \tau^- \tau^+}$ are multiplied by a factor $\cos\theta_A$, where $\cos\theta_A$ is defined by

$$a_1 = \cos\theta_A a_{\text{MSSM}} + \sin\theta_A a_S, \qquad (1.2)$$

where a_1 is the lightest of the two *CP*-odd scalars in the model. Above, a_{MSSM} is the *CP*-odd (doublet) scalar in the MSSM sector of the NMSSM and a_S is the additional *CP*-odd singlet scalar of the NMSSM. In terms of $\cos\theta_A$,

---

[1] A convenient program for exploring the NMSSM Higgs sector is NMHDECAY [14,15].

$C_{a_1\mu^-\mu^+} = C_{a_1\tau^-\tau^+} = C_{a_1b\bar{b}} = \cos\theta_A \tan\beta$ and $C_{a_1t\bar{t}} = \cos\theta_A \cot\beta$. Quite small values of $\cos\theta_A$ are natural when m_{a_1} is small as a result of being close to the $U(1)_R$ limit of the model. In the most general Higgs model, $C_{a\mu^-\mu^+}$, $C_{a\tau^-\tau^+}$, $C_{ab\bar{b}}$, and $C_{at\bar{t}}$ will be more complicated functions of the vevs of the Higgs fields and the structure of the Yukawa couplings. In this paper, we assume $C_{a\mu^-\mu^+} = C_{a\tau^-\tau^+} = C_{ab\bar{b}}$ and $C_{ab\bar{b}}/C_{at\bar{t}} = \tan^2\beta$.

For the analysis presented in this paper, we neglect the possible presence of large corrections at large $\tan\beta$ to $C_{ab\bar{b}}$ from SUSY loops [16–18]. These are typically character-ized by the quantity Δ_b which is crudely of order $(\mu\tan\beta)/(16\pi^2 M_{\text{SUSY}})$. The correction to the coupling takes the form of $1/(1 + \Delta_b)$. Since μ can have either sign, $C_{ab\bar{b}}$ can be either enhanced or suppressed relative to equality with $C_{a\tau^-\tau^+}$ (the corrections to which are much smaller) and $C_{a\mu^-\mu^+}$ (the corrections to which are negli-gible). This same correction factor would apply to $C_{a_1b\bar{b}}$ in the NMSSM case.

Key ingredients in understanding current limits are the branching ratios for $a \rightarrow \tau^+\tau^-$ and $a \rightarrow \mu^+\mu^-$ decays. These branching ratios are plotted in Figs. 1 and 2. (It is important to note that at tree level the a branching ratios apply equally to the a_1, independent of $\cos\theta_A$, due to the absence of tree level $a, a_1 \rightarrow VV$ couplings, and similar.) Note that $\text{BR}(a \rightarrow \tau^+\tau^-)$ and $\text{BR}(a \rightarrow \mu^+\mu^-)$ change very little with increasing $\tan\beta$ at any given m_a once $\tan\beta \gtrsim 2$. We note that in the region $m_a < 2m_\tau$, $\text{BR}(a \rightarrow \mu^+\mu^-)$ has some significant structures that arise from the fact that $\text{BR}(a \rightarrow gg)$ is substantial and varies rapidly in that region. The rapid variation in $\text{BR}(a \rightarrow gg)$ occurs when m_a crosses the internal quark loop thresholds. At higher m_a, $\text{BR}(a \rightarrow gg)$ becomes significant for m_a near $2m_b$. We plot $\text{BR}(a \rightarrow gg)$ in Fig. 3. Note that in the calculation of $\text{BR}(a \rightarrow gg)$ we have chosen to keep the loop quark masses equal to the current quark masses in our
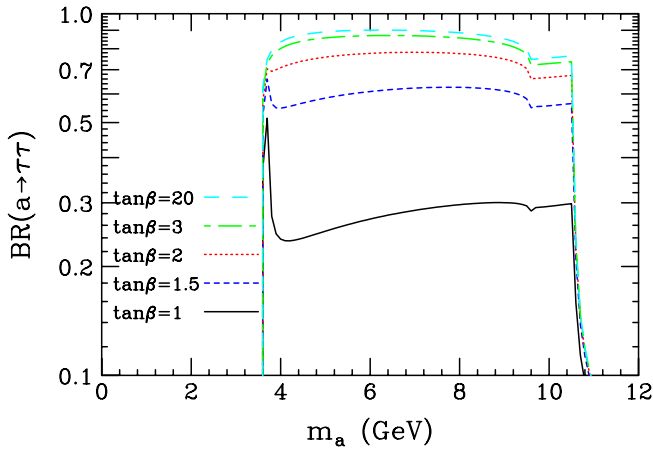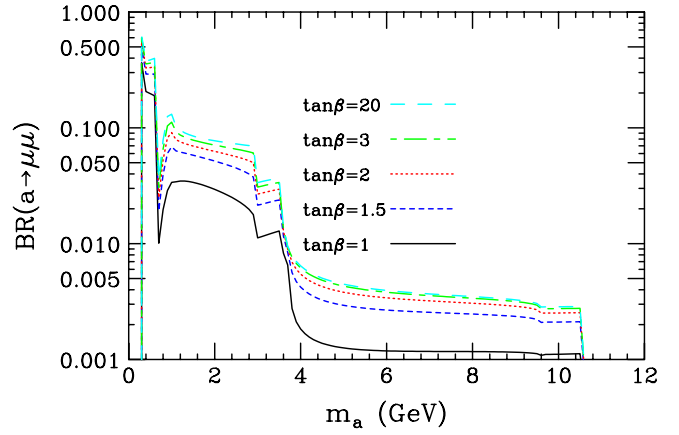

FIG. 2 (color online). $\text{BR}(a \rightarrow \mu^+\mu^-)$ is plotted as a function of m_a for a variety of $\tan\beta$ values. $\text{BR}(a \rightarrow \mu^+\mu^-)$ is independent of $\cos\theta_A$.

calculations, whereas we employ thresholds of $2m_K$ and $2m_D$ for the strange quark and charm quark final states, respectively. Some changes in the structures present, espe-cially in $\text{BR}(a \rightarrow \mu^+\mu^-)$, take place if, instead, the loop quark masses are set equal to the true physical threshold masses.

Of course, the above branching ratios are impacted by the $a \rightarrow c\bar{c}$ and $a \rightarrow s\bar{s}$ channels, the latter being a rather important competitor for smaller $\tan\beta$ and $m_a > 2m_K$. Plots of these branching ratios appear in Figs. 4 and 5, respectively.

It is relevant to note that both $\text{BR}(a \rightarrow \mu^+\mu^-)$ and $\text{BR}(a \rightarrow \tau^+\tau^-)$ tend to decline slowly as m_a is increased, with a significant dip in the latter for m_a close to $2m_b$, where the b-loop contribution to the gga coupling is close to the point at which the internal b's can go on shell. This has important implications for using these channels to probe the 9 GeV $\lesssim m_a \lesssim 2m_B$ region in which many pa-rameter choices lead to absence of light-a_1 fine-tuning in the NMSSM. "Light-a_1" fine-tuning is characterized nu-

FIG. 1 (color online). $\text{BR}(a \rightarrow \tau^+\tau^-)$ is plotted as a function of m_a for a variety of $\tan\beta$ values. $\text{BR}(a \rightarrow \tau^+\tau^-)$ is independent of $\cos\theta_A$.
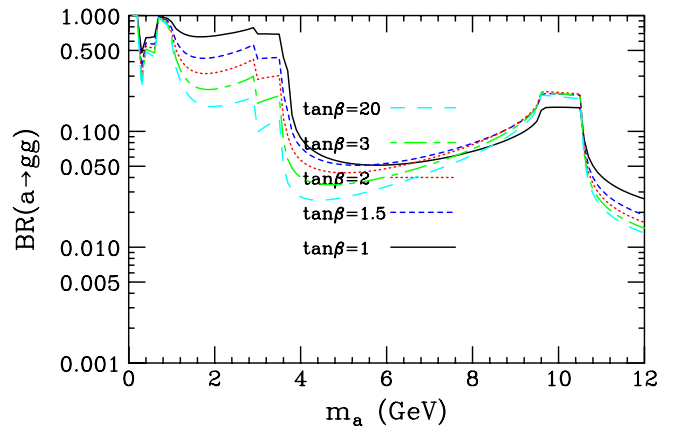

FIG. 3 (color online). $\text{BR}(a \rightarrow gg)$ is plotted as a function of m_a for a variety of $\tan\beta$ values.
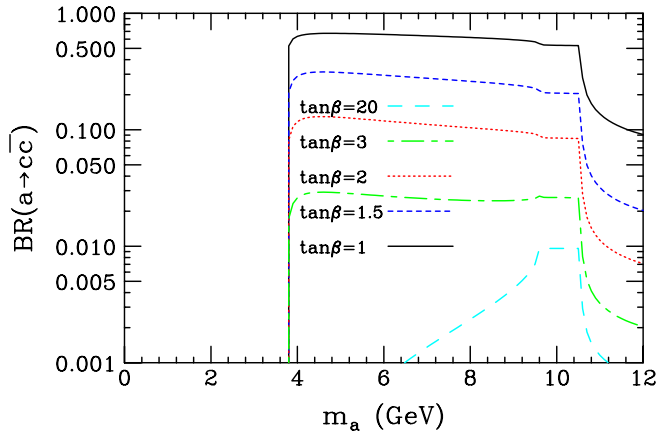
FIG. 4 (color online). BR($a \rightarrow c\bar{c}$) is plotted as a function of m_a for a variety of $\tan\beta$ values.

merically by a quantity we call G, defined in [3], that gives the degree of precision with which the A_λ and A_κ soft-SUSY-breaking NMSSM parameters must be chosen in order that $m_{a_1} < 2m_B$ *and* BR($h_1 \rightarrow a_1 a_1$) > 0.75 as required to allow $m_{h_1} \lesssim 105$ GeV to be consistent with published LEP constraints when the h_1 has SM-like $h_1 ZZ$ coupling. Absence of light-a_1 fine-tuning is equivalent to $G \lesssim 20$. Typically, this condition is satisfied only when the light a_1 of the NMSSM is mainly singlet. For example, at $\tan\beta = 10$, $0.6 \lesssim |C_{a_1 b\bar{b}}| \lesssim 1.2$ ($0.06 \lesssim |\cos\theta_A| \lesssim 0.12$) is required if $G < 20$ is imposed as well as requiring $m_{a_1} < 2m_B$ and BR($h_1 \rightarrow a_1 a_1$) > 0.75, with $G < 10$ achieved only for $\cos\theta_A \in [-0.08, -0.1]$, corresponding to $|C_{a_1 b\bar{b}}| \in [0.8, 1]$. The $G < 10$ range for $\tan\beta = 3$ is broader, $\cos\theta_A \in [-0.28, -0.08]$, while that for $\tan\beta = 50$ is narrow, $\cos\theta_A \in [-0.04, -0.06]$, yielding $|C_{a_1 b\bar{b}}| \in [0.24, 0.84]$ and $|C_{a_1 b\bar{b}}| \in [2, 3]$, respectively. Thus, lower $\tan\beta$ values will be harder to probe using direct limits on the a_1.
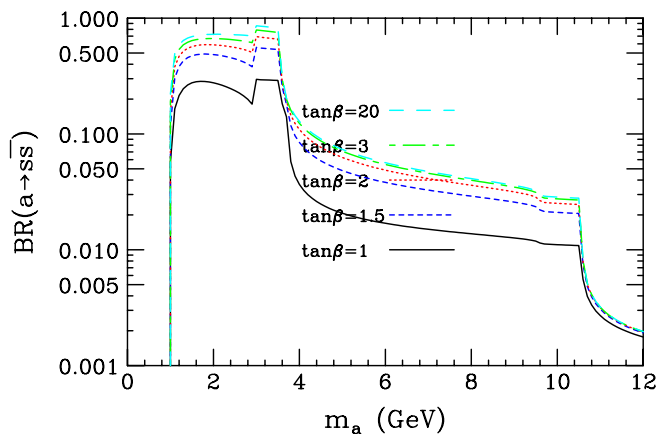

FIG. 5 (color online). BR($a \rightarrow s\bar{s}$) is plotted as a function of m_a for a variety of $\tan\beta$ values.

We emphasize that, given the importance of the exact a or a_1 branching ratios in the analyses that follow, additional attention to the most precise predictions possible is warranted. Our a, a_1 decay results employ a branching ratio program that is taken from HDECAY [19]. We note that the a_1 branching ratios obtained using this program are somewhat different than those that one obtains using the a_1 decay formulas in the current version of NMHDECAY. In particular, the former often predicts smaller BR($a_1 \rightarrow \tau^+\tau^-$) than does the latter.

II. UPSILON DECAY LIMITS COMPARED TO NMSSM PREDICTIONS

Before continuing with the general analysis, it is useful to compare the limits of [9,10] with the predictions of the NMSSM. This comparison is done for the same two types of scans as in the earlier paper [20], except that here we focus on the $3S$ state rather than the $1S$ state. In both scans, we hold the gaugino soft-SUSY-breaking parameters of the NMSSM fixed at $M_{1,2,3}(m_Z) = 100, 200, 300$ GeV and fix $\tan\beta$. In the first type of scan, called a "fixed-μ scan," we scan over the NMSSM soft-SUSY-breaking Higgs potential parameters A_λ and A_κ keeping the effective μ parameter of the model fixed at the representative value of $\mu = 150$ GeV (at $\tan\beta = 10$ and 50) or $\mu = 152$ GeV (at $\tan\beta = 3$ for which we must take $\mu = 152$ GeV in order to get physically allowable scenarios). In addition, in the fixed-μ scans we have kept the scalar soft-SUSY-breaking masses fixed at a common value of $M_{\text{SUSY}} = 300$ GeV and the A soft-SUSY-breaking parameters fixed to a common value of -300 GeV. In the second type of scan, termed a "full scan," we have allowed μ to vary and have also allowed the soft-SUSY-breaking scalar masses and A parameters to vary (independently of one another). In the full scan results presented, we have kept only scenarios with very low electroweak fine-tuning, as characterized by the parameter F (see [1] for more details) being smaller than 15, where $F < 15$ corresponds to absence of electroweak fine-tuning. $F < 15$ scenarios only arise for $m_{h_1} \lesssim 105$ GeV and are thus automatically ideal in the precision electroweak sense. As part of the fixed-μ scans and the full scans, we have required that the *CP*-even h_1 escape published LEP limits by virtue of dominant $h_1 \rightarrow a_1 a_1 \rightarrow 4\tau$ or 4-jet decays. In the forthcoming plots, the left-hand windows correspond to fixed-μ scan results and the right-hand windows give the results of a full scan for the same $\tan\beta$ value.

Our results for the $\tau^+\tau^-$ final state are shown in Fig. 6 and those for the $\mu^+\mu^-$ final state are shown in Fig. 7. Let us focus first on the $\tau^+\tau^-$ final state. The 90% C.L. BR($\Upsilon(3S) \rightarrow \gamma a$) $\times$ BR($a \rightarrow \tau^+\tau^-$) limits from *BABAR* range from $\sim 10^{-5}$ at m_a just above $2m_\tau$ with a long plateau at the 3–7 $\times 10^{-5}$ until m_a passes above 10 GeV where the limit is of order 10^{-4}. In Fig. 6, the black points have high m_{a_1} (8.8 GeV < $m_{a_1} \leq 2m_B$), the light grey
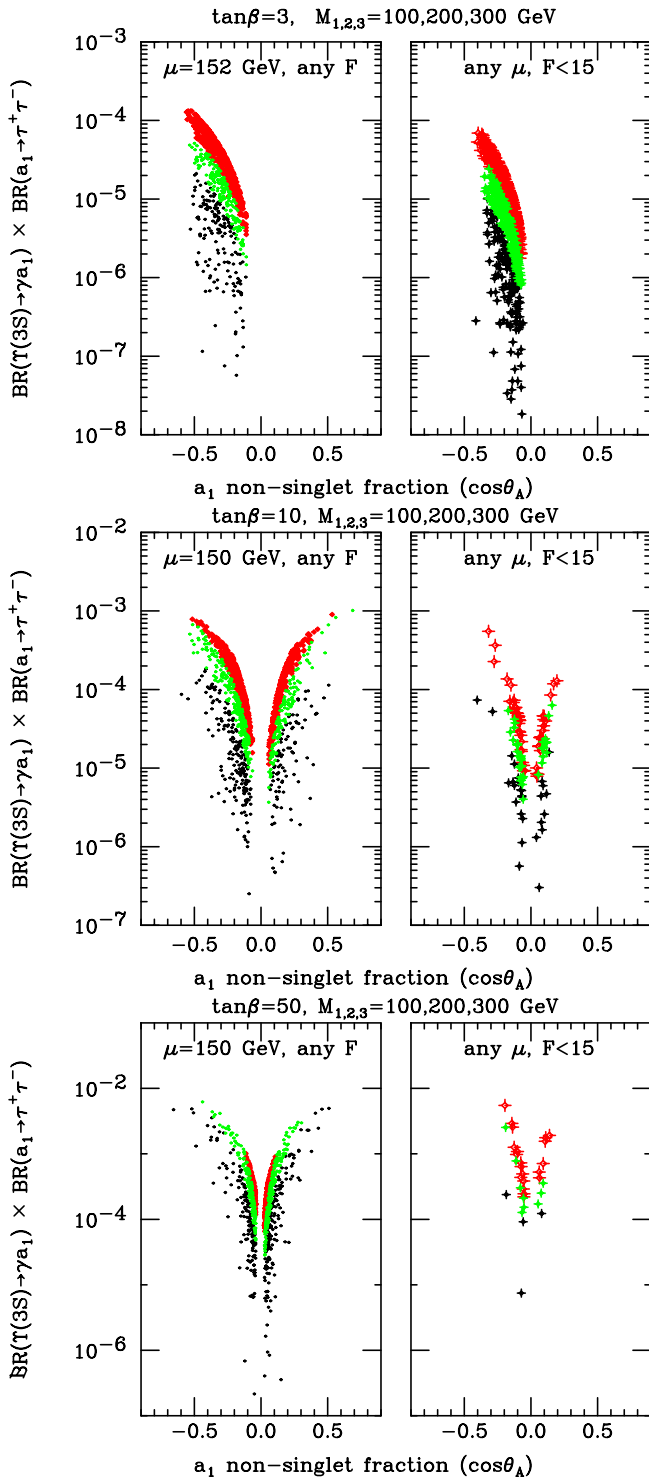
FIG. 6 (color online).   BR($\Upsilon(3S) \to \gamma a_1$) $\times$ BR($a_1 \to \tau^+\tau^-$) for NMSSM scenarios with various ranges for m_{a_1}: medium grey (red) = $2m_\tau < m_{a_1} < 7.5$ GeV; light grey (green) = 7.5 GeV $< m_{a_1} < 8.8$ GeV; and black = 8.8 GeV $< m_{a_1} < 2m_B$ GeV. The plots are for $\tan\beta = 3$, 10, 50, respectively. The left-hand window in each plot shows results for a fixed-μ scan as defined in the text (and in Ref. [20]) The right-hand window shows results for $F < 15$ points found using a "full scan" as defined in the text.

(green) points have 7.5 GeV $< m_{a_1} \lesssim 8.8$ GeV, and the medium grey (red) points have $2m_\tau < m_{a_1} \lesssim 7.5$ GeV. Let us first discuss $\tan\beta = 10$ results, since these can be com-
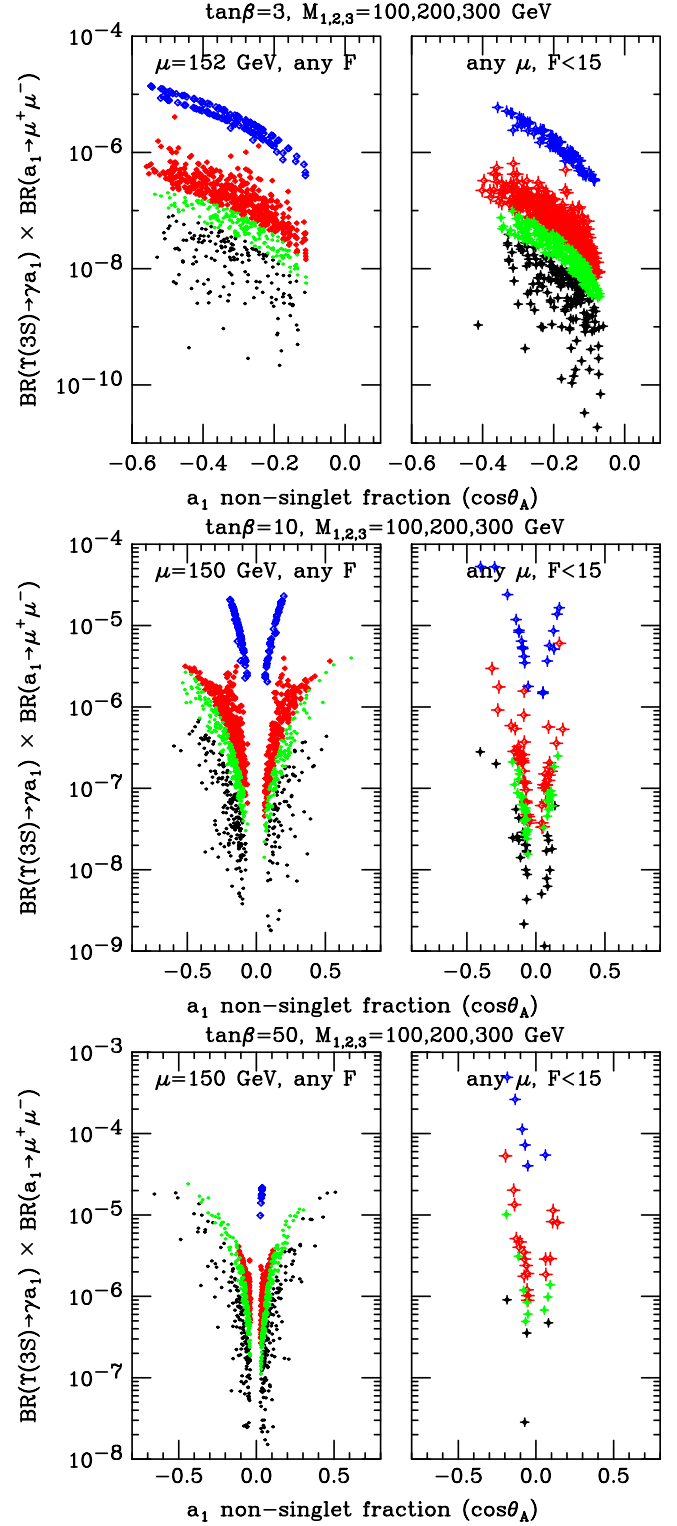

FIG. 7 (color online).   We plot BR($\Upsilon(3S) \to \gamma a_1$) $\times$ BR($a_1 \to \mu^+\mu^-$) using the same notation and scanning procedures as described in the caption of Fig. 6.

pared to those for $\Upsilon(1S) \to \gamma a_1 \to \gamma \tau^+ \tau^-$ presented in Ref. [20]. From comparing the *BABAR* limits summarized above with the relevant plot of Fig. 6, we see that most of the $m_{a_1} < 7.5$ GeV points are excluded, about half of the 7.5 GeV $< m_{a_1} \le 8.8$ GeV are excluded, but that many fewer of the $m_{a_1} > 8.8$ GeV points are excluded. Still, exclusions of this higher m_{a_1} region are much superior to those from the CLEO-III $\Upsilon(1S)$ data [21], which excluded none of the black points, a small fraction of the green points, and about half of the red points. This ability to probe to higher m_{a_1} using the $\Upsilon(3S)$ is particularly relevant in the NMSSM context since the GUT-scale tunings of A_λ and A_κ needed to obtain $m_{a_1} < 2m_B$ while at the same time having BR($h_1 \to a_1 a_1$) $\gtrsim 0.7$, as required in the ideal Higgs scenario, are minimal for m_{a_1} values close to $2m_B$. For $\tan\beta = 50$, one finds that almost all the $2m_\tau < m_{a_1} < 8.8$ GeV scenarios are excluded, but that lots of $m_{a_1} > 8.8$ GeV points survive. In contrast, for $\tan\beta = 3$ the *BABAR* results only significantly constrain the region $2m_\tau < m_{a_1} \le 7.5$ GeV.

We now turn to the $\mu^+ \mu^-$ final state. The 90% C.L. BR($\Upsilon(3S) \to \gamma a$) $\times$ BR($a \to \mu^+ \mu^-$) limits from *BABAR* are ~ 1–3.5×10^{-6} for $m_a \lesssim 1$ GeV, ~ 1–2×10^{-6} for $1 \lesssim m_a < 2m_\tau$, ~ 1–3×10^{-6} for $2m_\tau \lesssim m_a \lesssim 7.5$ GeV, and ~ 1–5×10^{-6} for 7.5 GeV $\lesssim m_{a_1} \lesssim 9.2$ GeV. In Fig. 7 the black points have high m_{a_1} (8.8 GeV $< m_{a_1} \le 2m_B$), the light grey (green) points have 7.5 GeV $< m_{a_1} \le$ 8.8 GeV, the medium grey (red) points have $2m_\tau < m_{a_1} \le$ 7.5 GeV, and the darker grey (blue) points have $m_{a_1} < 2m_\tau$. At $\tan\beta = 3$, the $\mu^+ \mu^-$ final state data eliminates more than 4/5 of the NMSSM model points in the $m_{a_1} < 2m_\tau$ mass range, but only a small number of the NMSSM points for $2m_\tau < m_{a_1} < 7.5$ GeV and none of the points with 7.5 GeV $\lesssim m_{a_1}$. At $\tan\beta = 10$, all $m_{a_1} < 2m_\tau$ NMSSM points are eliminated by the $\mu^+ \mu^-$ data as well as a small fraction of the $2m_\tau < m_{a_1} < 7.5$ GeV and 7.5 GeV $< m_{a_1} < 8.8$ GeV points, but none of the 8.8 GeV $< m_{a_1}$ points. At $\tan\beta = 50$, all $m_{a_1} < 2m_\tau$ NMSSM points are again eliminated, perhaps half of the $2m_\tau < m_{a_1} < 7.5$ GeV points are eliminated, a still significant fraction of the 7.5 GeV $< m_{a_1} < 8.8$ GeV points are eliminated, and even a significant number of the 8.8 GeV $< m_{a_1}$ points are eliminated.

To summarize, only the $\mu^+ \mu^-$ channel provides constraints for $m_{a_1} < 2m_\tau$ and almost all the ideal-Higgs-like NMSSM scenarios with $\tan\beta \ge 3$ are eliminated. For $2m_\tau < m_{a_1}$, the $\tau^+ \tau^-$ channel provides the most eliminations for all $\tan\beta$. Certainly, the *BABAR* $\Upsilon(3S)$ results are a big stride relative to the CLEO-III $\Upsilon(1S)$ results, especially at $m_{a_1} < 2m_\tau$ and at high m_{a_1}. Of course, it is important to note that the NMSSM scenarios most favored in order to minimize light-a_1 fine-tuning have m_{a_1} very near $2m_B$ and thus cannot be limited by Upsilon decays.

III. GENERAL LIMITS ON THE $ab\bar{b}$ COUPLING

Our ultimate goal is to use the Υ_{3S} limits in combination with other available limits to extract limits on $|C_{ab\bar{b}}|$. The older experiments that provide the most useful constraints are as follows. Prior to the recent *BABAR* data, for $2m_\tau < m_a < 9.2$ GeV the recent CLEO-III [21] limits on $\Upsilon(1S) \to \gamma a \to \gamma \tau^+ \tau^-$ were the strongest. For 9.2 GeV $< m_a < M_{\Upsilon(1S)}$, mixing of the a with various η_b and χ_0 bound states becomes crucial [22]. Reference [21] gives results for $C_{ab\bar{b}}^{\max}$ in this m_a range without taking this mixing into account but notes that their limits cannot be relied upon for $m_a > 9.2$ GeV. Whether additional limits can be extracted from lepton nonuniversality studies in the $9.2 < m_a < M_{\Upsilon(1S)}$ region is being studied [23]. OPAL limits [24] [which assume BR($a \to \tau^+ \tau^-$) $= 1$] on $e^+ e^- \to b\bar{b}\tau^+ \tau^-$ become numerically relevant for roughly 9 GeV $< m_a < 2m_B$. Reference [24] converts these limits to limits on the $ab\bar{b}$ coupling using the modeling of [22]. These are the only LEP limits in the $M_{\Upsilon(3S)} < m_a < 2m_B$ range and continue to be relevant up to 12 GeV. Above $m_a = 2m_B$ these $ab\bar{b}$ coupling limits become quite weak due to the $\eta_b - a$ mixing uncertainties and the decrease of BR($a \to \tau^+ \tau^-$). For $m_a \gtrsim 12$ GeV, limits on the $ab\bar{b}$ coupling can be extracted from $e^+ e^- \to b\bar{b}a \to b\bar{b}b\bar{b}$ [25]. One should also keep in mind that values of $|C_{ab\bar{b}}|$ above 50 raise issues of nonperturbativity of the $ab\bar{b}$ coupling and are likely to be in conflict with Tevatron limits on $b\bar{b}a$ production [26]. The limits, $C_{ab\bar{b}}^{\max}$, on $C_{ab\bar{b}}$ coming from all data, including the recent *BABAR* results, are plotted in Fig. 8 for various $R_{b/t} \equiv \sqrt{C_{ab\bar{b}}/C_{at\bar{t}}}$ values. (In a 2HDM model type-II context, $R_{b/t} = \tan\beta$.) Note the rapid deterioration as $m_a \to M_{\Upsilon(3S)}$. The variation with $R_{b/t}$ arises because BR($a \to \tau^+ \tau^-$) varies with $R_{b/t}$
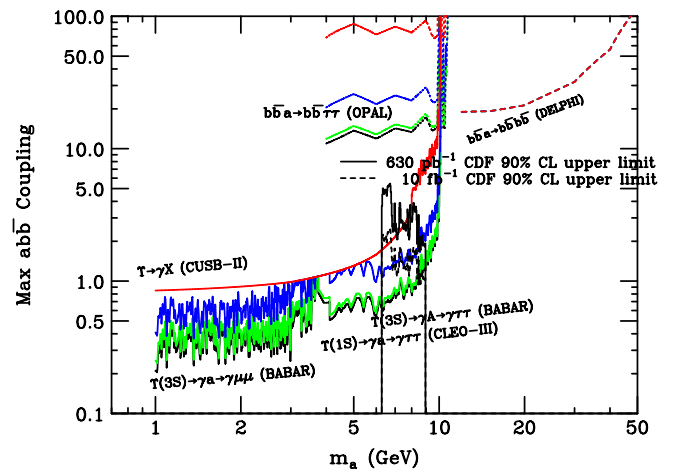

FIG. 8 (color online). Upper limit, $C_{ab\bar{b}}^{\max}$, on $|C_{ab\bar{b}}|$ as a function of m_a for a variety of $\tan\beta$ values coming directly from experimental data. The highest (red) curve is for $\tan\beta = 0.5$, the other curves, in order of decreasing $C_{ab\bar{b}}^{\max}$, are for $\tan\beta = 1$, $\tan\beta = 2$, and $\tan\beta \ge 3$.

as shown in Fig. 1. Basically, for $\tan\beta > 1$ the *BABAR* results provide the most stringent limits. For $\tan\beta = 0.5$ the a decays to a complicated mix of channels and the old CUSB-II limits (which were independent of the exact a final state) are strongest for $m_a \lesssim 8$ GeV.

In Fig. 8, we have also plotted limits extracted [27] from Tevatron data using a reinterpretation of a CDF analysis performed over the range 6.3 GeV $\le M_{\mu^+\mu^-} \le 9$ GeV [28,29]. This analysis placed limits on the ratio $R = [\sigma(\epsilon)\mathrm{BR}(\epsilon \to \mu^+\mu^-)]/[\sigma(\Upsilon_{1S})\mathrm{BR}(\Upsilon_{1S} \to \mu^+\mu^-)]$, where ϵ was a narrow resonance produced in the same manner as the Υ_{1S}. Fluctuations of R above a smooth fit to the overall spectrum were searched for and 90% C.L. limits were placed on R. It is relatively straightforward to apply this analysis to place limits on $R = [\sigma(a)\mathrm{BR}(a \to \mu^+\mu^-)]/[\sigma(\Upsilon_{1S})\mathrm{BR}(\Upsilon_{1S} \to \mu^+\mu^-)]$. The 90% C.L. limits on R corresponding to the available $L = 630$ pb^{-1} data set are then easily converted to limits on $|C_{ab\bar b}|$. These limits as a function of m_a are those plotted as the solid histogram. A simple statistical extrapolation of these limits to $L = 10$ fb^{-1} (an integrated luminosity that will soon be available) is shown as the dashed histogram. These limits hold for $\tan\beta > 2$. We see that these limits improve rapidly as m_a increases. While the $L = 630$ pb^{-1} limits are not quite competitive with the limits from *BABAR* data at $m_a \sim 9$ GeV, we observe that the $L = 10$ fb^{-1} limits will actually be slightly better if the extrapolation holds.

While $\Upsilon(nS)$-based limits are kinematically limited and become weak for $m_a \gtrsim 9.6$ GeV, there is no such kinematic limitation for limits based on hadronic collider data. In fact, CDF measured the $M_{\mu^+\mu^-}$ spectrum above 9 GeV, but did not perform the easily reinterpreted R analysis in the region $M_{\mu^+\mu^-} > 9$ GeV. In [27], we estimated the 90% C.L. limits from the $L = 630$ pb^{-1} measurements in the $M_{\mu^+\mu^-} > 9$ GeV region (out to $M_{\mu^+\mu^-} = 12$ GeV) and found that, in the range 9.6 GeV $\lesssim m_a \lesssim 2m_B$, implied limits on $|C_{ab\bar b}|$ were of order $|C_{ab\bar b}| < 1.6$–1.8 for m_a outside the Υ_{2S} and Υ_{3S} peaks. At both peaks we found $|C_{ab\bar b}| \lesssim 2$. For $L = 10$ fb^{-1}, these limits should come down to $|C_{ab\bar b}| \lesssim 1$, and begin to constrain the most preferred NMSSM parameter regions, especially for large $\tan\beta$.

IV. IMPLICATIONS OF GENERAL $ab\bar b$ LIMITS FOR NMSSM SCENARIOS

In the NMSSM, we note that it is always possible to choose $\cos\theta_A$ so that the limits on $C_{a_1b\bar b}$ as a function of $\tan\beta$ are satisfied. The maximum allowed value of $|\cos\theta_A|$, $\cos\theta_A^{\max}$, as a function of $m_a = m_{a_1}$ for various $\tan\beta$ values is plotted in Fig. 9. Constraints are strongest for $m_a \lesssim 9$ GeV for which Upsilon limits are relevant, and deteriorate rapidly above that. As seen in Fig. 8, currently the limits from the Tevatron/CDF data are not as strong
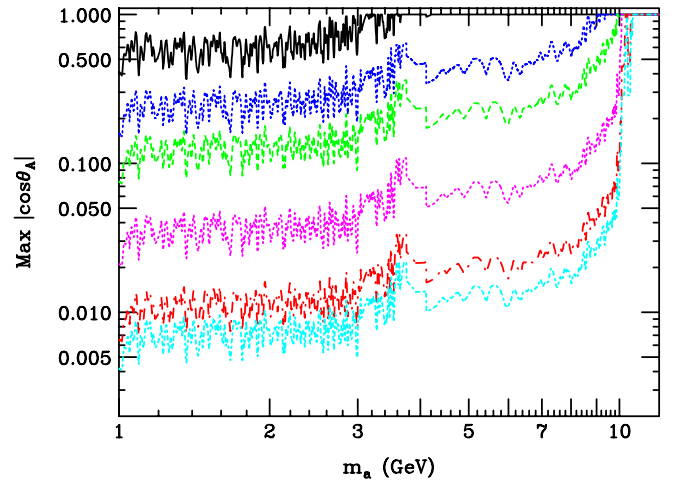

FIG. 9 (color online). $\cos\theta_A^{\max}$ in the NMSSM (where $C_{ab\bar b} = \cos\theta_A \tan\beta$) as a function of m_a. The different curves correspond to $\tan\beta = 1$ (upper curve), 1.7, 3, 10, 32, and 50 (lowest curve). CDF/Tevatron constraints do not affect this plot.

as those from the *BABAR* Υ_{3S} data and do not affect this plot.

As an aside regarding the general 2HDM(II) model, we note that any point for which $\cos\theta_A^{\max}$ is smaller than 1 corresponds to an m_a and $\tan\beta$ choice that is not consistent with the experimental limits. Disallowed regions emerge in the range $m_a \lesssim 2m_\tau$ for $\tan\beta = 1$, rising quickly to $m_a \lesssim 9$ GeV for $\tan\beta = 1.7$ and $m_a \lesssim 10$ GeV for $\tan\beta \gtrsim 3$. These excluded regions apply to any light doublet CP-odd Higgs boson, including the beyond the MSSM scenarios of [30–32] which are consistent with other experimental constraints for $\tan\beta \lesssim 2.5$.

We can illustrate the effects of the limits plotted in Fig. 9 on preferred NMSSM scenarios. Relevant plots appear below. The first set of plots, Figs. 10–12, for $\tan\beta = 3$, 10, and 50, respectively, show results for fixed-μ scans (see earlier definition). In each figure, the left-hand plot gives the light-a_1 fine-tuning measure G as a function of $\cos\theta_A$ before imposing the $\cos\theta_A^{\max}$ constraint while the right-hand plot gives G as a function of $\cos\theta_A$ after imposing $\cos\theta_A^{\max}$. The point notation is according to m_{a_1}: blue for $m_{a_1} < 2m_\tau$, red for $2m_\tau < m_{a_1} < 7.5$ GeV, green for 7.5 GeV $< m_{a_1} < 8.8$ GeV, and black for 8.8 GeV $< m_{a_1} < 2m_B$. We see that the bulk of points with $m_{a_1} < 7.5$ GeV are eliminated by the $\cos\theta_A^{\max}$ limit and that the points with $m_{a_1} > 7.5$ GeV at large $|\cos\theta_A|$ are also eliminated.

The second set of plots below, Figs. 13–15, shows results for "full scans," as defined previously, for $\tan\beta = 3$, 10, and 50, respectively. Only points with electroweak fine-tuning measure F below 15 are plotted. As in the previous set of plots, the left-hand plot in each figure shows the points allowed without the $\cos\theta_A^{\max}$ constraint and the right-hand plot displays the points remaining after impos-
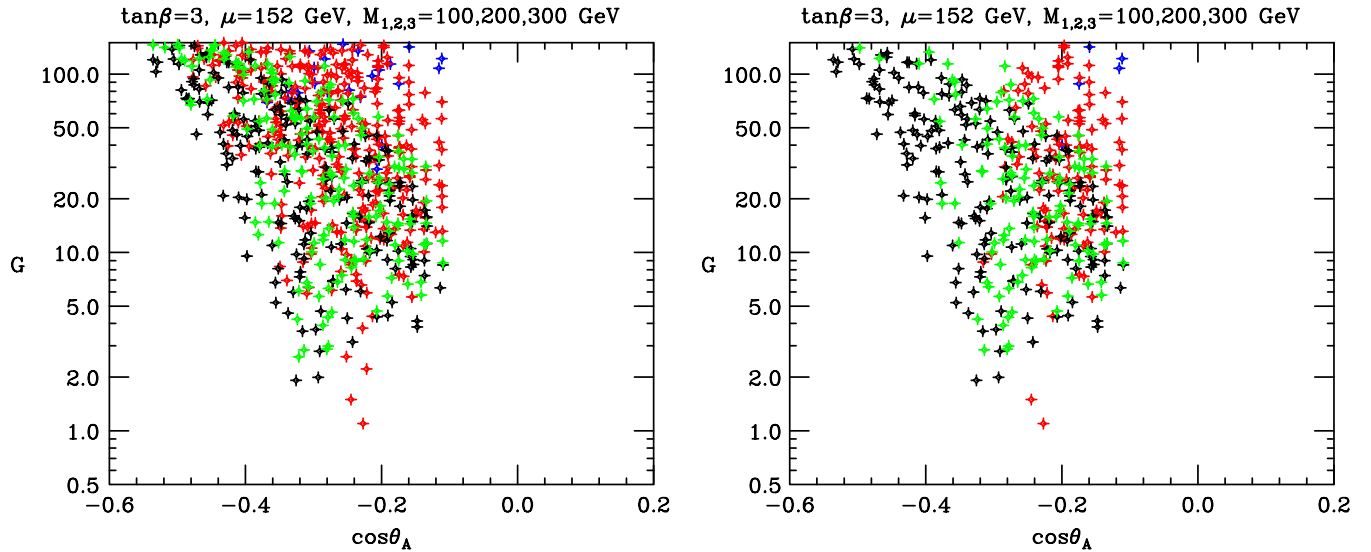
FIG. 10 (color online).   Light-a_1 fine-tuning measure G before and after imposing limits $|\cos\theta_A| \leq \cos\theta_A^{\max}$. These plots are those obtained for fixed-μ scans with $\mu = 152$ GeV and setting $\tan\beta = 3$. Note that many points with low m_{a_1} and large $|\cos\theta_A|$ are eliminated by the $|\cos\theta_A| < \cos\theta_A^{\max}$ requirement, including almost all the $m_{a_1} < 2m_\tau$ (blue) points and a good fraction of the $2m_\tau < m_{a_1} < 7.5$ GeV (red) points.

ing $\cos\theta_A^{\max}$. The limited statistics for the parameter scans that search for points with low F are apparent, but the trends are clearly the same as in the fixed μ scans presented previously.

From a theoretical perspective, an interesting pattern emerges: the $\cos\theta_A^{\max}$ constraint eliminates those points for which the light-a_1 fine-tuning measure G is never small and zeros in on those $\cos\theta_A$ values for which small G is quite likely.

V. EFFECTIVE ξ^2 IN THE $h \to 4\tau$ CHANNEL FOR VECTOR-BOSON FUSION AT THE LHC AND LEP Zh CHANNEL CONSTRAINTS

Discovery of a Higgs using vector-boson fusion at the LHC or at LEP with $2m_\tau < m_{a_1} < 2m_B$ (which is the only kind of point that survives with $G < 20$) is essentially determined by

$$\xi^2 \equiv \left(\frac{g_{VV}^h}{g_{VV}^{h_{SM}}}\right)^2 \mathrm{BR}(h \to aa)[\mathrm{BR}(a \to \tau^+\tau^-)]^2. \quad (5.1)$$
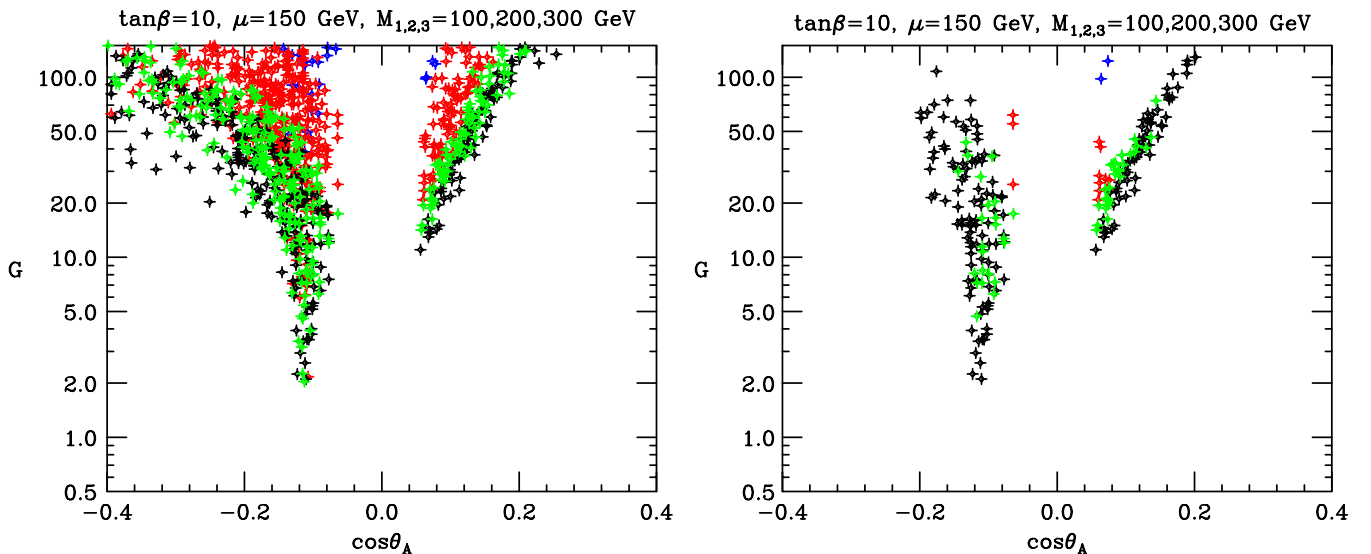

FIG. 11 (color online).   As in Fig. 10, but for $\mu = 150$ GeV and $\tan\beta = 10$. Note that many points with low m_{a_1} and large $|\cos\theta_A|$ are eliminated, including almost all the $m_{a_1} < 2m_\tau$ (blue) points and $2m_\tau < m_{a_1} < 7.5$ GeV (red) points.
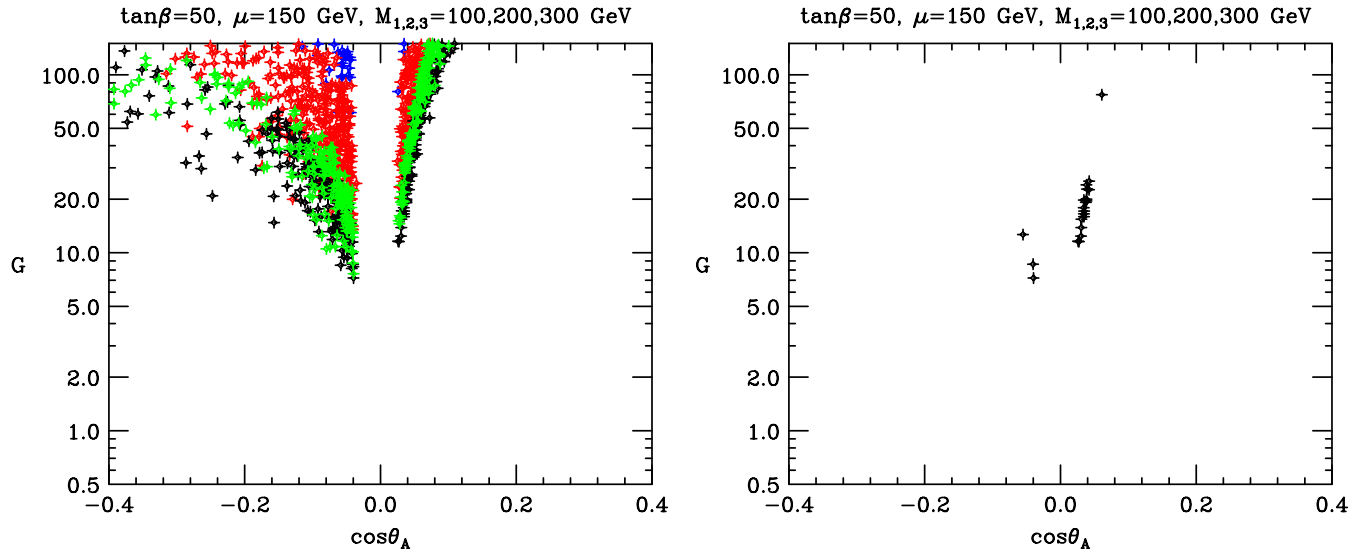
FIG. 12 (color online). As in Fig. 10, but for $\mu = 150$ GeV and $\tan\beta = 50$. Note that the only surviving points are those with $m_{a_1} > 8.8$ GeV (black points) at small $|\cos\theta_A|$.

We consider expectations for ξ^2 in the NMSSM ideal Higgs scenarios with the $\cos\theta_A^{\max}$ constraint imposed in addition to the usual constraints contained within NMHDECAY.

In Fig. 16 we take $\tan\beta = 3$ and plot ξ^2 for $h = h_1$ and $a = a_1$ as a function of m_{a_1} and as a function of m_{h_1} for points coming from the fixed-μ scans after imposing $G < 20$ and requiring $|\cos\theta_A| < \cos\theta_A^{\max}(m_a)$. We observe that ξ^2 as small as ~ 0.4 is possible at high m_{a_1}, which points tend to have $m_{h_1} \in [90, 100]$ GeV. As seen in Fig. 17,

these same remarks apply also to the $F < 15$ points obtained in our fine-tuning scans when $G < 20$ and $|\cos\theta_A| < \cos\theta_A^{\max}(m_{a_1})$ are imposed. These same remarks also apply to the $\tan\beta = 10$ plots of Figs. 18 and 19 as well as to the $\tan\beta = 50$ fixed-μ-scan plot of Fig. 20. (Note that no $F < 15$, $G < 20$ points survived our limited statistics electroweak fine-tuning scan in the $\tan\beta = 50$ case and so there is no corresponding figure.)

In addition, we have also considered ξ^2 expectations in scenarios with rather low $\tan\beta$. These were detailed in
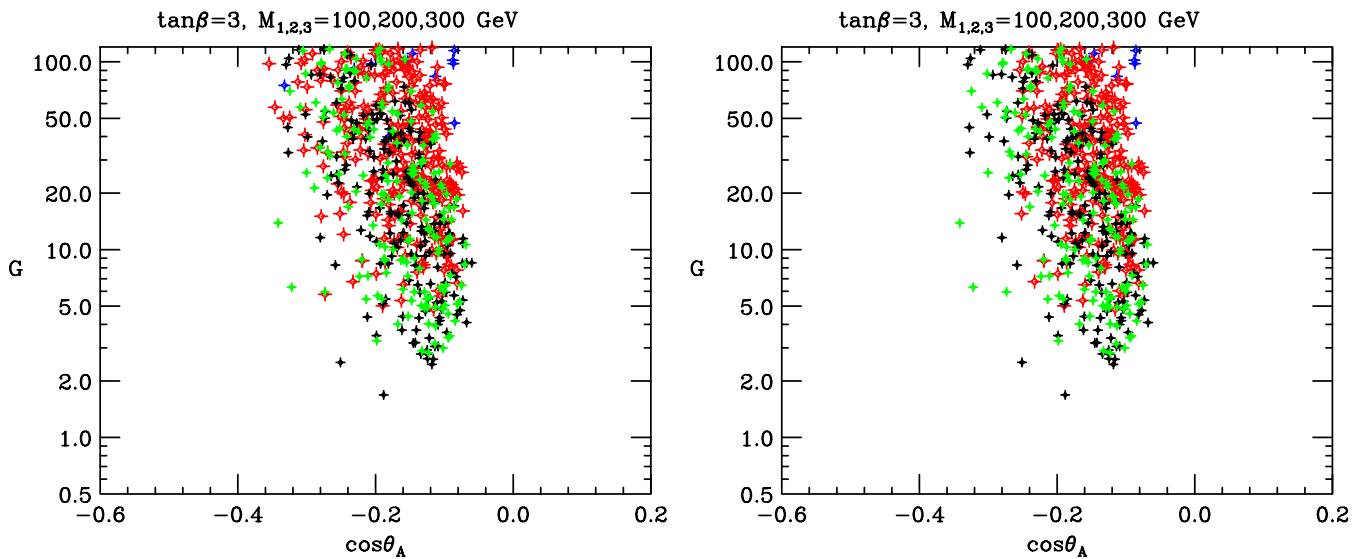

FIG. 13 (color online). Light-a_1 fine-tuning measure G before and after imposing $|\cos\theta_A| \leq \cos\theta_A^{\max}$. These are the results obtained using a "full scan" at $\tan\beta = 3$. Only solutions with electroweak fine-tuning measure $F < 15$ are retained. Note that a good fraction of the $m_{a_1} < 2m_\tau$ (blue) points and $2m_\tau < m_{a_1} < 7.5$ GeV (red) points are eliminated by the $\cos\theta_A^{\max}$ cut.
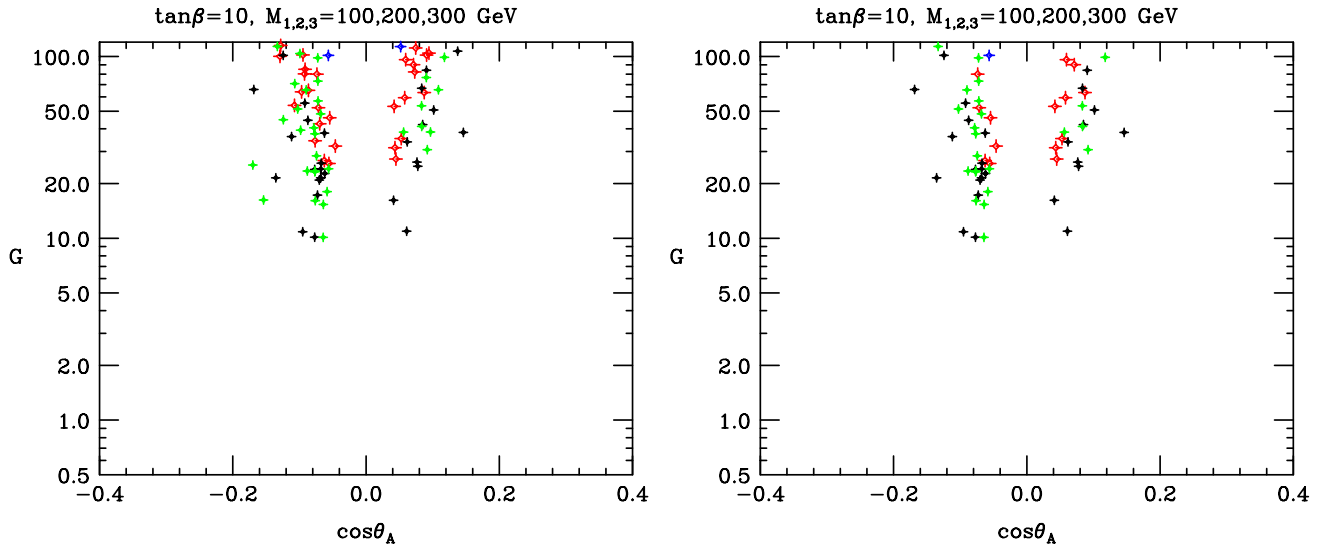
FIG. 14 (color online).   As in Fig. 13, but for $\tan\beta = 10$. Note that many points with lower m_{a_1} and large $|\cos\theta_A|$ are eliminated by the $|\cos\theta_A| \leq \cos\theta_A^{\max}$ cut.
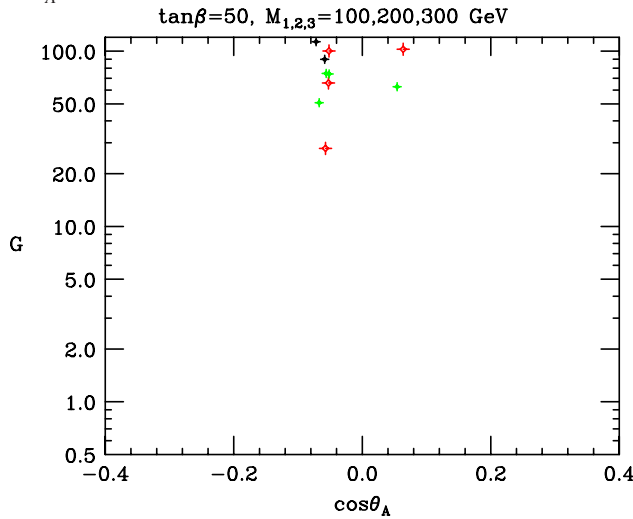

FIG. 15 (color online).   As in Fig. 13, but for $\tan\beta = 50$. Note that no $F < 15$ points found in our scans survive the $|\cos\theta_A| < \cos\theta_A^{\max}$ limits.
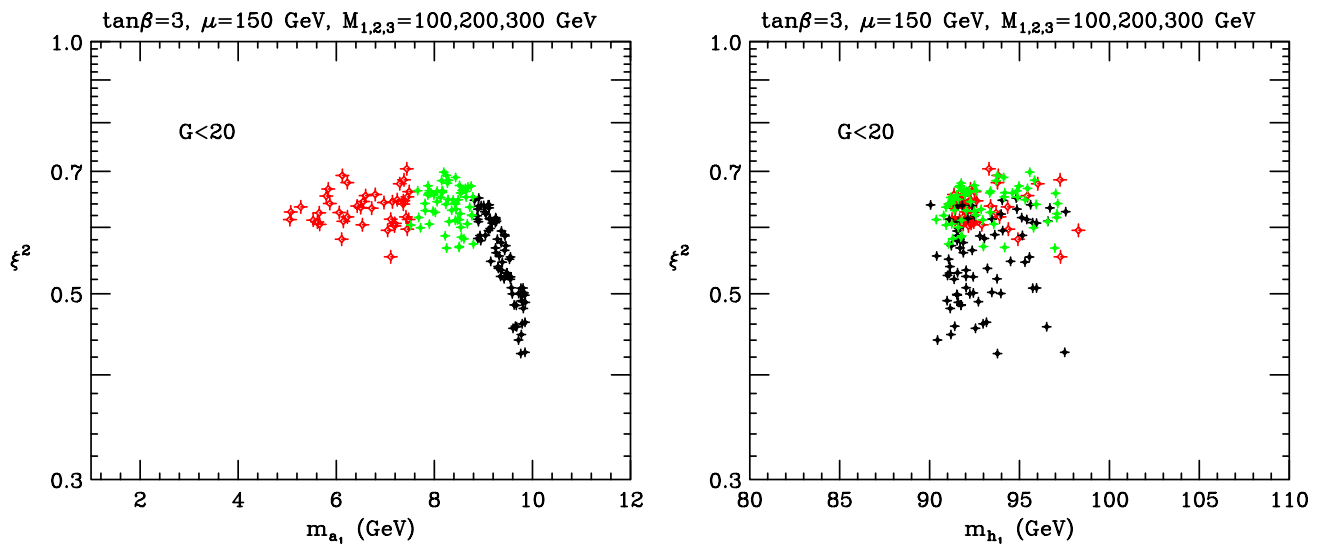

FIG. 16 (color online). ξ^2 for $h = h_1$ as a function of m_{a_1} and m_{h_1} for points with $G < 20$ and $|\cos\theta_A| < \cos\theta_A^{\max}(m_a)$. These plots are those obtained using the fixed-μ scanning procedure for $\tan\beta = 3$.
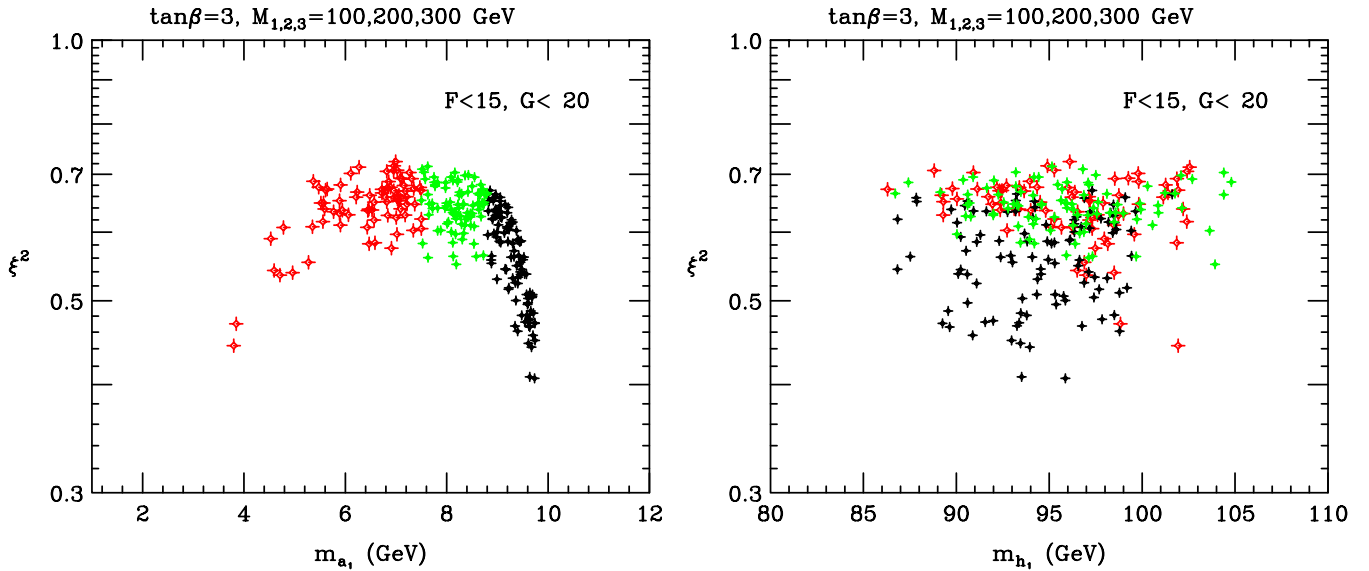
FIG. 17 (color online). ξ^2 for $h = h_1$ as a function of m_{a_1} and m_{h_1} for points with $F < 15$, $G < 20$, and $|\cos\theta_A| < \cos\theta_A^{\max}(m_a)$. These plots are those obtained using the described scanning procedure for $\tan\beta = 3$.
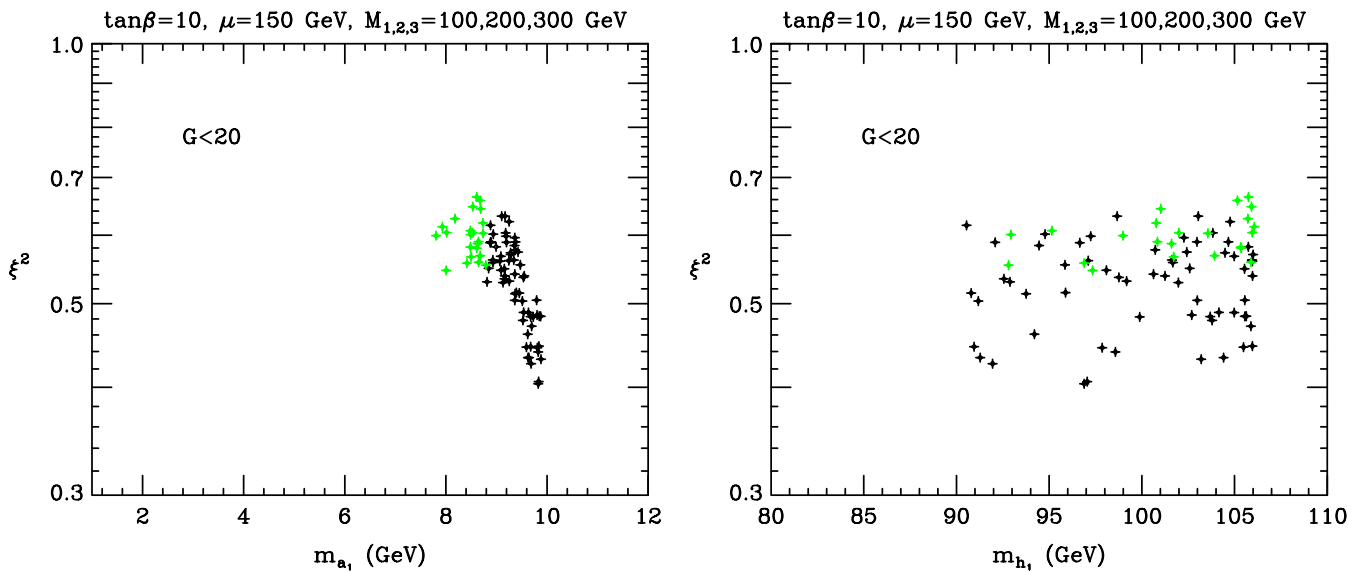

FIG. 18 (color online). ξ^2 for $h = h_1$ as a function of m_{a_1} and m_{h_1} for points with $G < 20$ and $|\cos\theta_A| < \cos\theta_A^{\max}(m_a)$. These plots are those obtained using the fixed-μ scanning procedure for $\tan\beta = 10$.

[33]. There, we performed fixed-μ scans as defined earlier, with the difference that at $\tan\beta = 1.7$ and $\tan\beta = 1.2$ we used different values for M_{SUSY} and A parameters, which values are indicated on the figures. At $\tan\beta = 2$ we employed $M_{\mathrm{SUSY}} = -A = 300$ GeV as for the fixed-μ scans for $\tan\beta = 3, 10, 50$.

The main distinguishing characteristic of the low $\tan\beta$ scenarios is that both h_1 and h_2 can be light with masses not far from 100 GeV, although there are certainly choices for the NMSSM parameters for which only h_1 is light while h_2 is much heavier. When h_2 is light, the charged Higgs $H^{\pm}$ can also have mass close to 100 GeV.[2] Here, our interest is in the predictions for ξ^2.

––––––––––
[2]Note that a light $H^{\pm}$ can cause the NMSSM prediction for $\mathrm{BR}(b \to s\gamma)$ to substantially exceed the experimental value, which is only slightly above the SM value. Thus, contributions from other SUSY diagrams must enter to cancel the $H^{\pm}$ diagrams. In models with low fine-tuning, SUSY is light and such a cancellation is generically entirely possible.
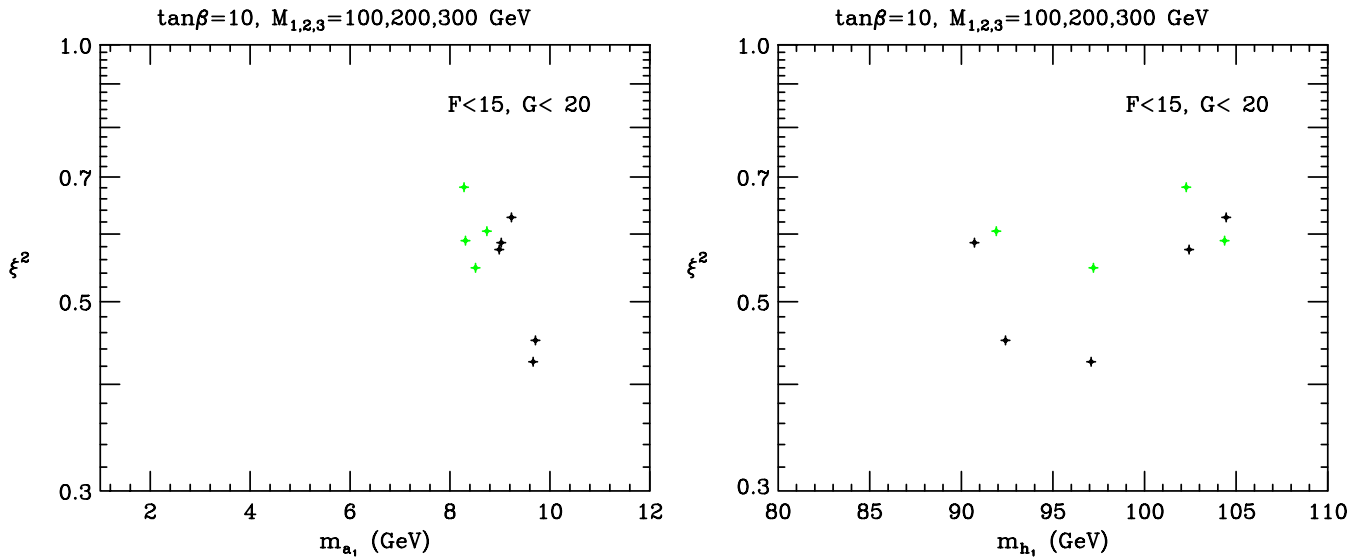
FIG. 19 (color online). ξ^2 for $h = h_1$ as a function of m_{a_1} and m_{h_1} for points with $F < 15$, $G < 20$, and $|\cos\theta_A| < \cos\theta_A^{\max}(m_a)$. These plots are those obtained using a "full scan" for $\tan\beta = 10$.

Results for ξ_1^2 at $\tan\beta = 2$ are rather similar to those found for higher $\tan\beta$, as shown in Fig. 21. In this figure, the blue $+$'s are all points that satisfy the NMHDECAY constraints—unlike the previous figures, color coding is not employed to distinguish different m_{a_1} values. Results for ξ_2^2 are not shown; even when m_{h_2} is close to 100 GeV, ξ_2^2 is quite small. This $\tan\beta = 2$ case is similar to the $\tan\beta = 3$, 10, 50 cases also in that it is almost always the case that VV couples primarily to the h_1 so that when $m_{h_1} \lesssim 105$ GeV we have the ideal Higgs explanation of the precision electroweak data.

For $\tan\beta \lesssim 1.7$, there are some interesting new subtleties compared to $\tan\beta \gtrsim 2$. Plots of ξ_1^2 of the h_1 and ξ_2^2 of h_2 appear in Figs. 22 and 23, respectively. In these plots, we follow the notation established in Ref. [33]. In detail, the blue $+$'s are all points that satisfy the NMHDECAY constraints. The red crosses single out those points for which $m_{h_1} < 65$ GeV. Yellow squares indicate points for which BR($h_1 \rightarrow a_1 a_1$) < 0.7. In [33], there were also points indicated by green diamonds for which *in addition* the light *CP*-odd Higgs is primarily doubletlike, $\cos^2\theta_A > 0.5$. However, these are absent from the present plots, not because of the improved $\cos\theta_A^{\max}$ limits from the recent
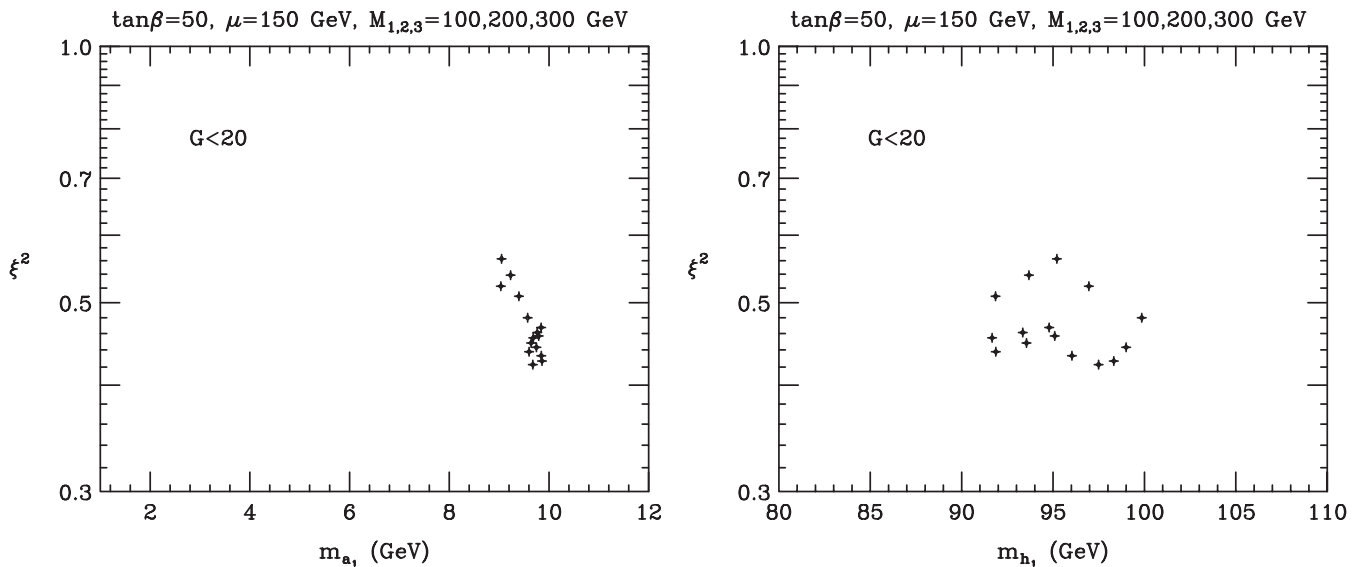

FIG. 20. ξ^2 for $h = h_1$ as a function of m_{a_1} and m_{h_1} for points with $G < 20$ and $|\cos\theta_A| < \cos\theta_A^{\max}(m_a)$. These plots are those obtained using the fixed-μ scanning procedure for $\tan\beta = 50$.
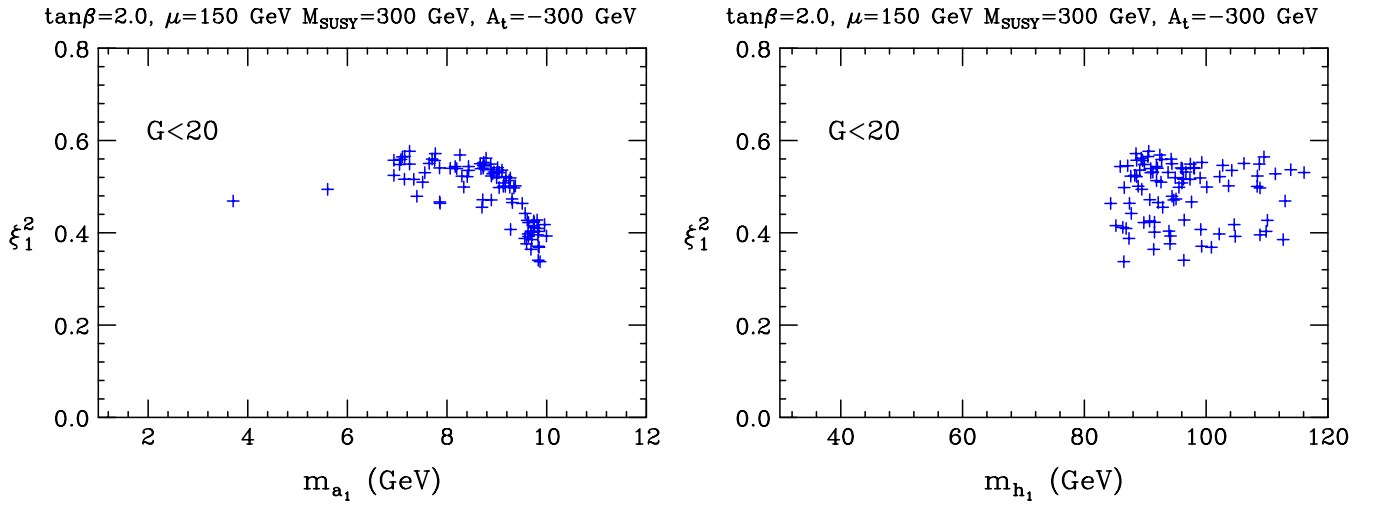
FIG. 21 (color online). ξ_1^2 as a function of m_{a_1} and m_{h_1} for points with $G < 20$ and $|\cos\theta_A| < \cos\theta_A^{\max}(m_{a_1})$ and $\tan\beta = 2$. These plots are those obtained using a fixed-μ scanning procedure with the μ, M_{SUSY}, and A parameters indicated on the figure. We have not indicated different m_{a_1} mass ranges using different colors in these figures.
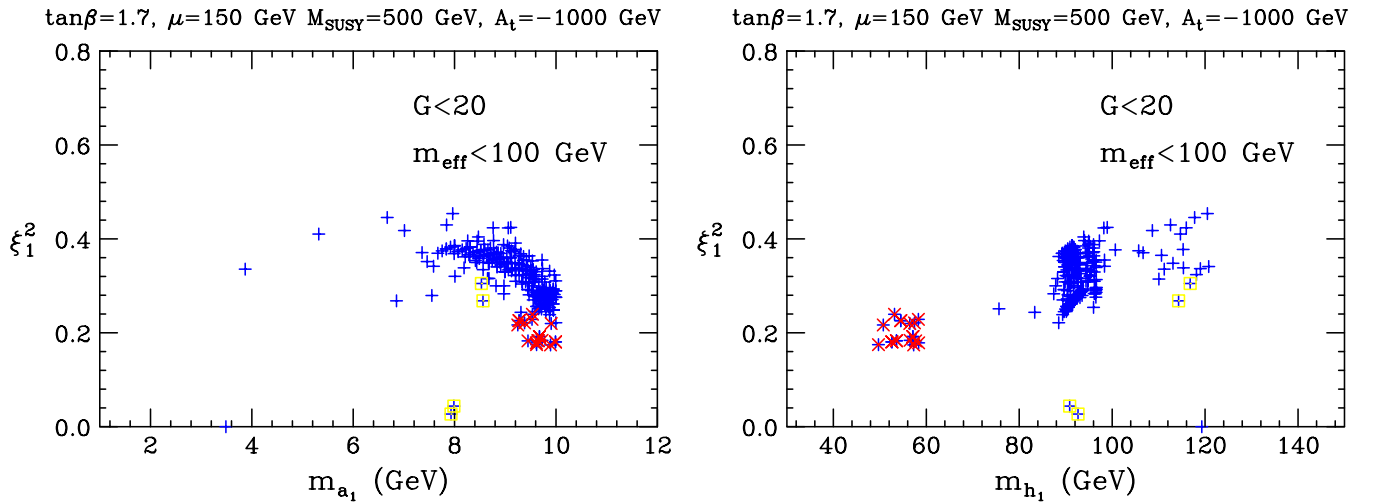

FIG. 22 (color online). ξ_1^2 as a function of m_{a_1} and m_{h_1} for $\tan\beta = 1.7$ points obtained from a fixed-μ scan after requiring $G < 20$, $m_{\mathrm{eff}} < 100$ GeV, and $|\cos\theta_A| < \cos\theta_A^{\max}(m_{a_1})$. The point notation is explained in the text.

BABAR data, but rather because of the $G < 20$ requirement which very strongly disfavors large $|\cos\theta_A|$ at all m_{a_1}, including m_{a_1} above $M_{\Upsilon(3S)}$. Of course, the *BABAR* data eliminates many points with $m_{a_1} < M_{\Upsilon(3S)}$ having $\cos^2\theta_A < 0.5$, certainly more than in the analysis of [33].

Let us now discuss the $\tan\beta = 1.7$ case in more detail. We first wish to discuss the extent to which the points that survive the NMHDECAY scans can be ideal in the precision electroweak sense. Defining

$$CV_1 = g_{VVh_1}/g_{VVh_{\mathrm{SM}}}, \qquad CV_2 = g_{VVh_2}/g_{VVh_{\mathrm{SM}}}, \quad (5.2)$$

then, noting that it is a good approximation to neglect any h_3 coupling to VV, one has the sum rule

$$CV_1^2 + CV_2^2 \simeq 1. \tag{5.3}$$

In this notation, the effective precision electroweak mass, m_{eff}, is given to very good approximation by

$$m_{\mathrm{eff}} = m_{h_1}^{CV_1^2} m_{h_2}^{CV_2^2}. \tag{5.4}$$

In order to guarantee that all accepted points are ideal, we require as part of our $\tan\beta = 1.7$ scan that $m_{\mathrm{eff}} < 100$ GeV.[3] Now, let us describe the associated plots, Figs. 22 and 23. First, very low values of m_{h_1} are possible (see the red crosses). These red cross points are such that ξ_1^2 and ξ_2^2 are comparable and both below 0.2.
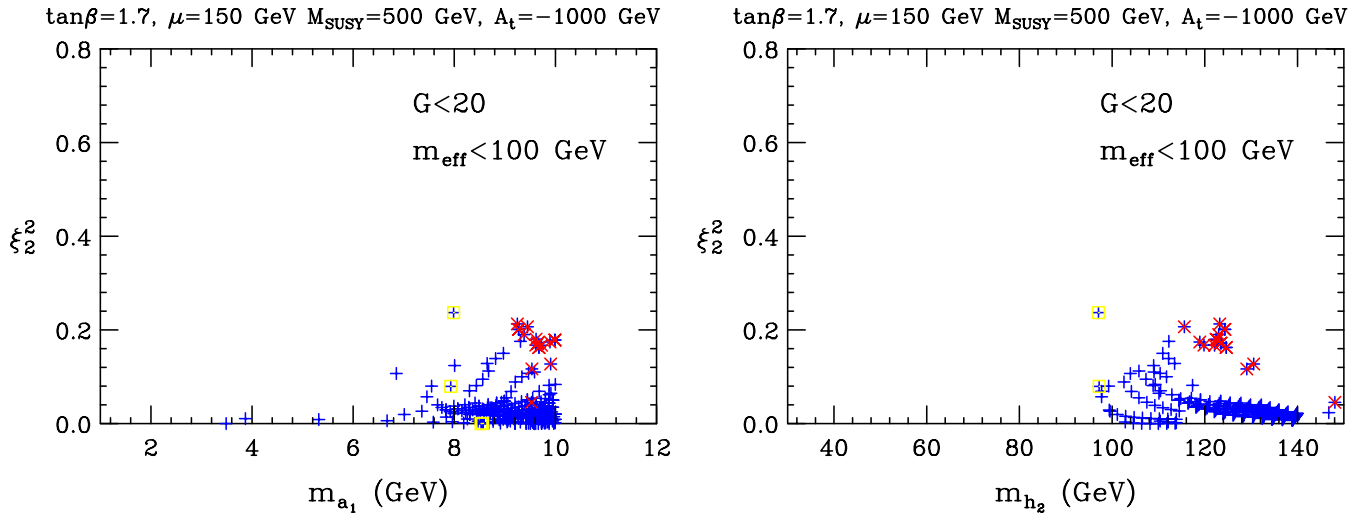
---

[3]This was not imposed in the plots of [33].

FIG. 23 (color online). ξ_2^2 as a function of m_{a_1} and m_{h_2} for $\tan\beta = 1.7$ points obtained from a fixed-μ scan after requiring $G < 20$, $m_{eff} < 100$ GeV, and $|\cos\theta_A| < \cos\theta_A^{max}(m_{a_1})$.

Second, very few of the yellow square points [defined by BR($h_1 \to a_1a_1$) < 0.7] survive the ideal requirement. But, those that do have quite small ξ_1^2 and ξ_2^2. The run-of-the-mill blue + points have somewhat larger $\xi_1^2 \lesssim 0.4$ and somewhat smaller $\xi_2^2 \lesssim 0.2$. Overall, the 4τ final state in h_1 and h_2 decays typically has a significantly smaller cross section for $\tan\beta = 1.7$ as compared to $\tan\beta \gtrsim 2$.

The lowest value of $\tan\beta$ consistent with maintaining perturbativity up to the GUT scale is $\tan\beta = 1.2$. ξ_1^2 and ξ_2^2 plots for this case appear in Figs. 24 and 25, respectively. In this case, the effective ξ_1^2 values are mostly quite small. Relative to the $\tan\beta = 1.7$ plots, the main thing that has changed is that BR($a_1 \to \tau^+\tau^-$) has declined substantially. The majority of the a_1 decays are into gg and $c\bar{c}$, i.e. final states that are harder to constrain.

Of course, the knowledgeable reader will recognize that all the ξ^2 plots presented are aimed at comparing these NMSSM models to the new ALEPH analysis of the 4τ final state [11]. According to the ALEPH analysis, to have $m_{h_1} \lesssim 100$ GeV, $\xi_1^2 \lesssim 0.52$ (0.42) is required if $m_{a_1} \sim 10$ GeV (4 GeV). These limits rise rapidly with increasing m_{h_1}—for $m_{h_1} = 105$ GeV (the rough upper limit on m_{h_1} such that electroweak fine-tuning remains quite small and precision electroweak constraints are fully satisfied) the ALEPH analysis requires $\xi^2 \lesssim 0.85$ ($\lesssim 0.7$) at $m_{a_1} \sim 10$ GeV (4 GeV). These limits are such that the easily viable NMSSM scenarios are ones: (i) with m_{a_1} below but fairly close to $2m_B$, which is, in any case, strongly preferred by minimizing the light-a_1 fine-tuning measure G; and/or (ii) with $\tan\beta$ relatively small
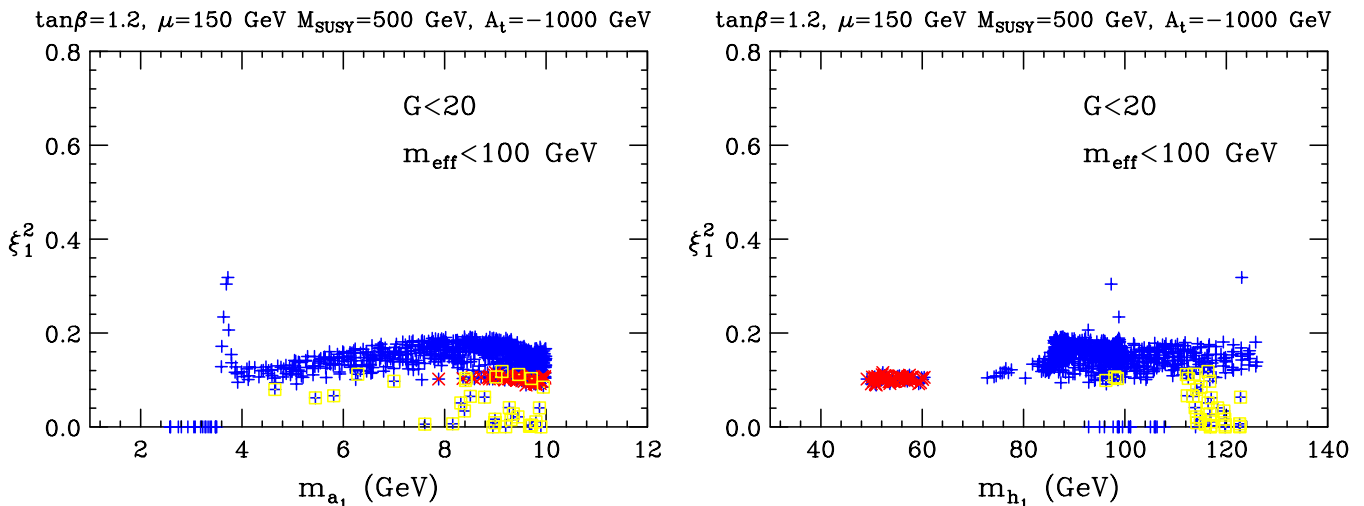

FIG. 24 (color online). ξ_1^2 as a function of m_{a_1} and m_{h_1} for $\tan\beta = 1.2$ points obtained from a fixed-μ scan after requiring $G < 20$, $m_{eff} < 100$ GeV, and $|\cos\theta_A| < \cos\theta_A^{max}(m_{a_1})$.
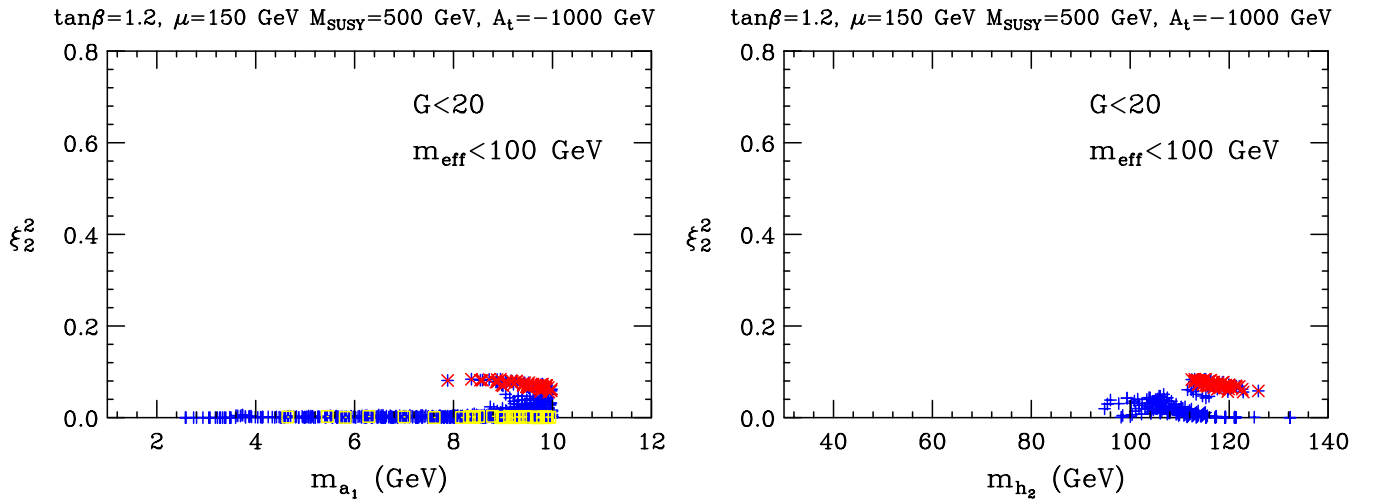
FIG. 25 (color online). ξ_2^2 as a function of m_{a_1} and m_{h_2} for $\tan\beta = 1.2$ points with $G < 20$, $m_{\mathrm{eff}} < 100$ GeV, and $|\cos\theta_A| < \cos\theta_A^{\max}(m_{a_1})$.

$(\lesssim 2)$.[4] These are also the scenarios for which Upsilon constraints are either weak or absent. In particular, we note the following: (a) all $\tan\beta \leq 2$ cases provide $m_{h_1} < 100$ GeV scenarios that escape the ALEPH limits; (b) there are a few $G < 20$, $\tan\beta = 3$ scenarios with m_{h_1} as large as 98 and 99 GeV and with ξ^2 essentially equal to the ALEPH limits of $\xi^2 \leq 0.42$ and $\xi^2 \leq 0.45$ applicable at these respective m_{h_1} values; (c) $\tan\beta = 10$ ideal scenarios easily allow for $m_{h_1} \sim 100$–105 GeV (because the tree-level Higgs mass is larger at $\tan\beta = 10$ than at $\tan\beta = 3$) and at $m_{a_1} \lesssim 2m_B$ many $m_{h_1} \gtrsim 100$ GeV points have $\xi^2 < 0.5$ in the fixed-μ scan and a few of the full-scan points have $\xi^2 < 0.6$ for $m_{h_1} \sim 105$ GeV, both of which are below the $m_{a_1} = 10$ GeV ALEPH upper limits on ξ^2 of 0.52 at $m_{h_1} \sim 100$ GeV and 0.85 at $m_{h_1} = 105$ GeV; (d) at $\tan\beta = 50$ there are some $G < 20$ points with $m_{h_1} \sim 100$ GeV and $m_{a_1} \lesssim 2m_B$ having ξ^2 below the 0.52 ALEPH limit. Finally, we note that for the entire range of Higgs masses studied, the ALEPH limits were actually $\sim 2\sigma$ stronger than expected. Thus, it is not completely unreasonable to consider the possibility that the weaker expected limits should be employed. These weaker limits for example allow ξ^2 as large as 0.52 at $m_{h_1} \sim 95$ GeV and 0.9 for $m_{h_1} \sim 100$ GeV. These weaker limits allow ample room for the majority of the $m_{a_1} \lesssim 2m_B$ ideal Higgs scenarios.

---

[4] A similar conclusion applies to models beyond the MSSM with a light doublet *CP*-odd Higgs boson [30–32]. Since these scenarios are consistent with other experimental limits only for $\tan\beta \lesssim 2.5$, the new preliminary ALEPH limits only constrain the upper range of the allowed region of $\tan\beta$.

VI. CONCLUSIONS

In this paper, we have updated the constraints on the NMSSM ideal Higgs scenarios in which h_1 (and for low $\tan\beta$, also possibly h_2) has mass $\lesssim 105$ GeV and decays largely (but not entirely) via $h_1 \to a_1 a_1 \to \tau^+\tau^-\tau^+\tau^-$. Such low mass(es) for the Higgs boson(s) with large VV coupling are strongly preferred by precision electroweak data and are also strongly preferred in order to minimize electroweak fine-tuning. Indeed, all the NMSSM points plotted in this paper have effective precision electroweak mass below ~ 105 GeV. The new data that constrains such scenarios derives from $\Upsilon_{3S} \to \gamma\mu^+\mu^-$ and $\gamma\tau^+\tau^-$ decay data from *BABAR* and ALEPH studies of the $e^+e^- \to Z4\tau$ final state.

The latter was employed by ALEPH to place limits as a function of m_{h_1} and m_{a_1} on the quantity $\xi^2 \equiv \frac{\sigma(h_1)}{\sigma(h_{\mathrm{SM}})} \mathrm{BR}(h_1 \to a_1 a_1)[\mathrm{BR}(a_1 \to \tau^+\tau^-)]^2$. Although these new constraints are significant, there is still ample room for the ideal Higgs scenarios, especially if $\tan\beta$ is small and $m_{a_1} \lesssim 2m_B$ [the latter region being that for which the "light-a_1" fine-tuning measure is minimal and also $\mathrm{BR}(a_1 \to \tau^+\tau^-)$ is somewhat suppressed]. For $\tan\beta \geq 3$, it is only the $m_{a_1} \lesssim 2m_B$ points that can escape the ALEPH ξ^2 limits. The case of $\tan\beta = 3$ is the most marginal with only a few NMSSM points with $m_{h_1} \lesssim 99$ GeV (the rough upper limit on m_{h_1} at $\tan\beta = 3$) having ξ^2 essentially equal to the ALEPH limit at a given m_{h_1}. For $\tan\beta = 10$, one finds scenarios with $m_{h_1} \sim 100$–105 GeV and $\xi^2 \sim 0.43$ when $m_{a_1} \lesssim 2m_B$, which ξ^2 is well below the ALEPH limit of ~ 0.52–0.85 for such m_{h_1} and m_{a_1}. At $\tan\beta = 50$, although our scanning statistics were limited, we found points with $m_{h_1} \sim 100$ GeV and $m_{a_1} \lesssim 2m_B$ having ξ^2 below the 0.52 ALEPH limit. (We note that the ALEPH

limits are significantly stronger than the ALEPH collaboration was expecting. If one were to use expected limits instead then the $\tan\beta \lesssim 3$ scenarios would be much less constrained.) For $\tan\beta \lesssim 2$, the ideal-Higgs NMSSM scenarios are not particularly constrained by the ALEPH limits. In particular, for $\tan\beta = 2, 1.7, 1.2$ one finds $m_{h_1} \lesssim 100$ GeV scenarios with $\xi^2 \lesssim 0.32, 0.23, 0.15$, respectively. The lower ξ^2 values arise because these lower $\tan\beta$ values have increasingly reduced BR$(a_1 \to \tau^+\tau^-)$, which, in turn, is due to increasingly larger values of BR$(a_1 \to gg + c\bar{c})$. Such ξ^2 values are completely consistent with the ALEPH limits.

The Tevatron and LHC discovery prospects for the Higgs bosons in the low-tan β scenarios have yet to be fully analyzed. Searches for the h_1 and the a_1 using the $a_1 \to \tau^+\tau^-$ and $a_1 \to \mu^+\mu^-$ decay modes will certainly become more difficult as these branching ratios decline with decreasing $\tan\beta$. Such search modes include: direct (vs coming from $h_1 \to a_1 a_1$) detection of the a_1 at the Tevatron and LHC in the $gg \to a_1 \to \mu^+\mu^-$ channel [27]; searches for $gg \to h_1 \to a_1 a_1 \to \tau^+\tau^-\tau^+\tau^- + \tau^+\tau^-\mu^+\mu^-$ at the Tevatron [34] and LHC [35]; and LHC detection of $pp \to pph_1$ with $h_1 \to a_1 a_1 \to \tau^+\tau^-\tau^+\tau^-$ [36]. Backgrounds in the increasingly important channels with $a_1 \to gg + c\bar{c}$ will undoubtedly be much larger and will make discovery employing these latter a_1 decay modes quite difficult.

As part of the NMSSM study, we first obtained updated limits on the $ab\bar{b}$ coupling (assuming $C_{ab\bar{b}} = C_{a\tau^-\tau^+} = C_{a\mu^-\mu^+}$) that are applicable in a wide variety of model contexts. The main improvements in these general limits result from recent *BABAR* data.

Finally, one should not forget that the NMSSM is only the simplest model of a general category of SUSY models having one or more singlet scalar superfields in addition to the usual two-doublet scalar superfields. Such models are generically very attractive in that they allow for an NMSSM-like solution to the μ problem, while maintaining coupling constant unification and renormalization group evolution electroweak symmetry breaking as in the MSSM. In addition, models with more than one extra singlet scalar superfield will allow one or more light Higgs bosons with SM-like couplings to VV (a scenario having excellent agreement with precision electroweak constraints and minimal electroweak fine-tuning) that can escape Upsilon and LEP limits more easily than the NMSSM by virtue of multiple decays channels of the Higgs $\to a_k a_j, \ldots$ type.

ACKNOWLEDGMENTS

[1] R. Dermisek and J. F. Gunion, Phys. Rev. Lett. **95**, 041801 (2005).

[2] R. Dermisek and J. F. Gunion, Phys. Rev. D **73**, 111701 (2006).

[3] R. Dermisek and J. F. Gunion, Phys. Rev. D **75**, 075019 (2007).

[4] R. Dermisek and J. F. Gunion, Phys. Rev. D **76**, 095006 (2007).

[5] S. Chang, P. J. Fox, and N. Weiner, J. High Energy Phys. 08 (2006) 068.

[6] S. Chang, R. Dermisek, J. F. Gunion, and N. Weiner, Annu. Rev. Nucl. Part. Sci. **58**, 75 (2008).

[7] J. F. Gunion, J. High Energy Phys. 08 (2009) 032.

[8] F. Domingo, U. Ellwanger, E. Fullana, C. Hugonie, and M. A. Sanchis-Lozano, J. High Energy Phys. 01 (2009) 061.

[9] B. Aubert *et al.* (*BABAR* Collaboration), Phys. Rev. Lett. **103**, 181801 (2009).

[10] B. Aubert *et al.* (*BABAR* Collaboration), Phys. Rev. Lett. **103**, 081803 (2009).

[11] S. Schael *et al.* (The ALEPH Collaboration), arXiv:1003.0705.

[12] J. R. Ellis, J. F. Gunion, H. E. Haber, L. Roszkowski, and F. Zwirner, Phys. Rev. D **39**, 844 (1989).

[13] John F. Gunion, Howard E. Haber, Gordon Kane, and Sally Dawson, *The Higgs Hunter's Guide*, Frontiers in Physics (Perseus Books, New York, 2000), Vol. 80.

[14] U. Ellwanger, J. F. Gunion, and C. Hugonie, J. High Energy Phys. 02 (2005) 066.

[15] U. Ellwanger and C. Hugonie, Comput. Phys. Commun. **175**, 290 (2006).

[16] L. J. Hall, R. Rattazzi, and U. Sarid, Phys. Rev. D **50**, 7048 (1994).

[17] M. S. Carena, M. Olechowski, S. Pokorski, and C. E. M. Wagner, Nucl. Phys. **B426**, 269 (1994).

[18] D. M. Pierce, J. A. Bagger, K. T. Matchev, and R. J. Zhang, Nucl. Phys. **B491**, 3 (1997).

[19] A. Djouadi, J. Kalinowski, and M. Spira, Comput. Phys. Commun. **108**, 56 (1998).

[20] R. Dermisek, J. F. Gunion, and B. McElrath, Phys. Rev. D **76**, 051105 (2007).

[21] W. Love *et al.* (CLEO Collaboration), Phys. Rev. Lett. **101**, 151802 (2008).

[22] M. Drees and K. i. Hikasa, Phys. Rev. D **41**, 1547 (1990).

[23] M. A. Sanchis-Lozano, Mod. Phys. Lett. A **17**, 2265 (2002); Int. J. Mod. Phys. A **19**, 2183 (2004); E. Fullana and M. A. Sanchis-Lozano, Phys. Lett. B **653**, 67 (2007); M. A. Sanchis-Lozano, arXiv:0709.3647.

[24] G. Abbiendi *et al.* (OPAL Collaboration), Eur. Phys. J. C **23**, 397 (2002).

[25] The Delphi Collaboration, ICHEP Report No. DELPHI 2002-037-CONF-571, 2002. We employ Table 20—these are very close to those appearing in the figures of J. Abdallah *et al.* (DELPHI Collaboration), Eur. Phys. J. C **38**, 1 (2004).

[26] T. Aaltonen *et al.* (CDF Collaboration), Phys. Rev. Lett. **103**, 201801 (2009).

[27] R. Dermisek and J. F. Gunion, arXiv:0911.2460 [Phys. Rev. D (to be published)].

[28] G. Apollinari *et al.*, Phys. Rev. D **72**, 092003 (2005).

[29] T. Aaltonen *et al.* (CDF Collaboration), Eur. Phys. J. C **62**, 319 (2009).

[30] R. Dermisek, arXiv:0806.0847.

[31] R. Dermisek, AIP Conf. Proc. **1078**, 226 (2009).

[32] K. J. Bae, R. Dermisek, D. Kim, H. D. Kim, and J. H. Kim, arXiv:1001.0623.

[33] R. Dermisek and J. F. Gunion, Phys. Rev. D **79**, 055014 (2009).

[34] V. M. Abazov *et al.* (D0 Collaboration), Phys. Rev. Lett. **103**, 061801 (2009).

[35] M. Lisanti and J. G. Wacker, Phys. Rev. D **79**, 115006 (2009).

[36] J. R. Forshaw, J. F. Gunion, L. Hodgkinson, A. Papaefstathiou, and A. D. Pilkington, J. High Energy Phys. 04 (2008) 090.